

¹ Deep crustal architecture of the Parnaíba basin of
² NE Brazil from receiver function analysis:
³ Implications for basin subsidence.

⁴ Diogo L.O. Coelho^{1,*}, Jordi Julià^{1,2}, Verónica Rodríguez-Tribaldos³, Nicholas
⁵ White³

⁶ ¹*Programa de Pós-graduação em Geodinâmica e Geofísica, Universidade Federal do Rio
7 Grande do Norte, Lagoa Nova, Natal-RN, CEP 59078-970, Brazil*

⁸ ²*Departamento de Geofísica, Universidade Federal do Rio Grande do Norte, Lagoa Nova,
9 Natal-RN, CEP 59078-970, Brazil*

¹⁰ ³*Bullard Laboratories, Department of Earth Sciences, University of Cambridge, Madingley
11 Rise House, Madingley Road, Cambridge, CB3 0EZ, UK*

¹² *Corresponding author (e-mail: locdiogo@gmail.com)

¹³ **Abstract**

¹⁴ We investigate the crustal architecture of the Parnaíba basin of NE Brazil by analyzing
¹⁵ receiver functions along a ~600 km-long transect crossing the central portion of the
¹⁶ basin. The transect consisted of 9 broadband stations interspaced at ~70 km distance and
¹⁷ recording continuously for a period of ~6 months, with the goal of improving our under-
¹⁸ standing of the origin and evolution of this large cratonic basin. Our results reveal that
¹⁹ crustal structure is quite uniform along the transect, and consists of a 39 - 45 km thick
²⁰ crust with a smooth S-velocity increase with depth from 3.4 to 4.1 km/s. Bulk Vp/Vs
²¹ ratios vary between 1.69 and 1.76, with isolated occurrences of ratios slightly above 1.80.
²² The uniformity of the basin's underlying crust is consistent with minimal stretching of
²³ the lithosphere, as independently suggested by seismic profiling and surface geology. Bulk

24 Vp/Vs ratios and crustal velocities are consistent with a thin (5-6 km) layer of mafic ma-
25 terial in the lower crust, which is unlikely to have modified subsidence. Our results are
26 consistent with pure thermal subsidence of the basin, although convecting processes in the
27 underlying asthenosphere need to be investigated to fully assess its origin and evolution.

28

29 **Keywords:** Cratonic basin, Crustal architecture, South America

30

31 **Supplementary material:** [description of material] is available at <https://doi.org/xxxx>.
32 [GSL will assign the doi and url unless you already have one]

33 Introduction

34 The genesis and evolution of large basins in the stable interiors of continents is an impor-
35 tant geological problem that is not easily understood within the Plate Tectonics paradigm.
36 In spite of notable attempts by *Klein and Hsui (1987)* to link the formation of all cratonic
37 basins of Europe, Africa, North and South America to rifting and break-up of a Late Pre-
38 cambrian supercontinent, no single mechanism seems capable of explaining the development
39 of cratonic basins on such a large scale. This inability is nicely illustrated in *Kaminski and*
40 *Jaupart (2000)*, who showed that in spite of the four major cratonic basins of North America
41 - Hudson Bay, Michigan, Illinois, and Williston - having similar ages and being close to one
42 another, they exhibit different subsidence histories and are characterized by different time-
43 scales and sediment thicknesses. Adding to this complexity, is the intriguing observation
44 that prolonged intervals of slow subsidence alternate with fast subsidence rates (*Cloetingh*
45 *and Burrov, 2011*). Although periods of fast subsidence often coincide with orogenic activity
46 at plate boundaries, the impression remains that individual mechanisms might be needed

47 to understand the large variety of depositional histories in cratonic basins worldwide.

48 The Parnaíba basin of NE Brazil is one of three large Paleozoic basins in stable South
49 America - together with the Paraná basin of SE Brazil and the Amazon basin, in the northern
50 half of the continent. The basin is commonly described as a large, sag-type cratonic basin,
51 with a roughly circular shape and a depocenter reaching up to 3.5 km depth (*Góes and Feijó,*
52 *1994; Vaz et al., 2007; Daly et al., 2014*). It is generally agreed that initial subsidence of the
53 basin occurred in an intra-continental setting during Paleozoic times, with the proto-basin
54 being framed by three large cratonic masses (Figure 1): Amazon to the West, São Luiz-West
55 Africa to the North, and São Francisco-Congo to the South and East (*Almeida et al., 1981;*
56 *Brito Neves et al., 1984; Cordani et al., 2009; Brito Neves and Fuck, 2013; Cordani et al.,*
57 *2013*). The physical mechanism behind its subsidence and evolution, on the other hand,
58 is more controversial. A number of basin-forming mechanisms have been proposed for this
59 basin, which fall into one of two broad categories: (i) Thermally-driven subsidence, which
60 is based on a number of seismically identified unconformities in the sedimentary record of
61 the basin combined with evidence lacking for rifting structures (*Daly et al., 2014*); and (ii)
62 thermo-mechanical subsidence, which relies on the inference of graben-like structures in the
63 basin's basement from interpreted gravity, magnetic, and pseudo-gravity residual anomalies
64 (*Brito Neves et al., 1984; Nunes, 1993; Cordani et al., 1984; de Castro et al., 2014*).

65 Very little is known about the deep, crustal architecture of this enigmatic cratonic basin.
66 Most of our current knowledge is restricted to low-resolution, continental-scale studies (*Feng*
67 *et al., 2004; 2007; Lloyd et al., 2010; van der Meijde et al., 2013; Assumpção et al., 2013a;*
68 *2013b; Uieda and Barbosa, 2017*), and a single seismic reflection line crossing the basin
69 in the EW direction (*Daly et al., 2014*). Continental-scale studies showed the crust is
70 thinnest (30-35 km) under the Proterozoic provinces of South America, while thickest under

71 cratonic landmasses (e.g. Amazon and São Francisco, 41 ± 4 km) and cratonic basins (e.g.
72 Paraná and Parnaíba, 42 ± 4 km). More detailed information was developed from the
73 seismic reflection survey of *Daly et al. (2014)*, where a basin-wide migrated cross-section
74 demonstrated the presence of up to three different crustal blocks under the basin: a ~ 35 km
75 thick, highly reflective crustal block to the East, interpreted as the continuation of the
76 Proterozoic Borborema Province; a ~ 40 km thick, moderately reflective crustal block to
77 the West, identified as the Amazon craton; and a central, almost transparent crustal block
78 referred to as the Parnaíba block. Surprisingly, no crustal thickness estimates were reported
79 for the central Parnaíba block, as the reflection signature expected from the crust-mantle
80 boundary seemed to be absent in the migrated cross section.

81 In this work, we characterize the deep, crustal architecture of the Parnaíba basin by map-
82 ping subsurface seismic discontinuities with teleseismic P-wave receiver functions (*Langston,*
83 *1979*). We present estimates of crustal thickness and Vp/Vs ratio at 9 broadband stations
84 developed through the H κ -stacking procedure of *Zhu and Kanamori (2000)*, S-wave velocity-
85 depth profiles obtained from the joint inversion of receiver functions and surface-wave dis-
86 persion velocities (*Julia et al., 2000; 2003*), and a depth-migrated cross-section developed
87 with the Common Conversion Point (CCP) stacking of *Frassetto et al. (2010)*. The H κ -
88 stacking analysis reveals that the crust is 39-45 km thick and that bulk Vp/Vs ratios are in
89 the 1.69-1.76 range (although they may locally reach values of 1.80-1.82). The CCP stacking
90 migrated cross-section displays a relatively flat Moho at 38-44 km depth, consistent with the
91 H κ -stacking estimates. The velocity-depth profiles show the crust is simple, and consists of
92 a 2-3 km thick sedimentary package overlying a 3.4-3.6 km/s crust down to 25-30 km depth,
93 where S-velocities gradually increase to ~ 4.0 -4.1 km/s near Moho depths. The crust-mantle
94 boundary is gradational in character under most of the stations, and uppermost mantle

95 velocities are around 4.5 km/s. Our findings are consistent with models invoking minimal
96 stretching of the basin's underlying crust and thermal cooling as the driving mechanism for
97 subsidence. The role of deep convecting processes in the asthenosphere cannot be assessed
98 within our study and should be the focus of future studies.

99 Geology and Tectonic Setting

100 The depositional history of the Parnaíba basin is built on five primary tectono-sedimentary
101 sequences and two magmatic pulses separated by regional unconformities (*Góes and Feijó,*
102 *1994; Vaz et al., 2007*). The basin infill is characterized by thick epicontinental sequences,
103 which started with deposition of siliciclastic and volcanoclastic rocks in the Cambrian and
104 Ordovician periods. Deposition continued in the Silurian with alternating deposits of thin
105 and thick siliciclasts from continental and shallow marine environments, and then in the
106 Meso-Devonian/Carboniferous with deposits from a continental syneclide transitioning to
107 wards shallow marine environments. During Neocarboniferous/Permatriassic times, sedi-
108 ments again derived from a continental syneclide transitioning towards a shallow marine en-
109 vironment, showing signs of desertification towards the end of the period. A Juro-Cretaceous
110 sequence presents sediments deposited during the beginning of Pangea break-up. Two mag-
111 matic events of Early Jurassic and Early Cretaceous ages - expressed in the Mosquito and
112 Sardinha formations, respectively - are observed interfingering with basin strata, with major
113 volcanic exposures being found in the central portion of the basin and secondary exposures
114 outcropping in the northeast and southeast corners. Alluvial and aeolian deposits of Ceno-
115 zoic age cover large areas of the Parnaíba basin (see Figure 1).

116 The Parnaíba basin is framed by the Amazonian craton to the West, the São Francisco
117 craton to the Southeast, the São Luiz craton to the North, and the Proterozoic Borborema

Province to the East (Fig. 1). Two of these major cratonic blocks were part of larger cratonic landmasses (São Francisco-Congo and São Luiz-West Africa) that existed before the opening of the Atlantic ocean in Mesozoic times, and likely surrounded a central Parnaíba block presently concealed under the basin's sediments. The existence of a Parnaíba block was postulated from geophysical evidence, petrography, and Rb-Sr and K-Ar geochronology of basement rocks (*Cordani et al., 1984*), as well as from collisional tectonic models (*Brito Neves et al., 1984; Klein et al., 2008; Nunes, 1993*), and it was regarded as one of the continental fragments inherited by the South American platform after the dispersal of the Rodinia supercontinent (*Fuck et al., 2008*). Analysis of recent airborne magnetic and gravity surveys further subdivide the Parnaíba block into smaller fragments - Parnaíba North, Parnaíba South, and Teresina - which are characterized by marked changes in magnetic properties and by variations of up to 3.5 km in crustal thickness (*de Castro et al., 2014*).

The concealed Parnaíba block would have an approximately triangular shape and be delimited by up to three suture zones related to ancient collisions with the surrounding continental landmasses. To the West, the Araguaia suture zone would represent the final Neoproterozoic collision between the Amazonian craton and the Parnaíba block (*Fuck et al., 2008; Brito Neves and Fuck, 2014*); to the East, the Transbrasiliano Lineament - a continental-scale linear feature characterized by strong magnetic anomalies and slow lithospheric S-wave velocities - would mark the border with the Borborema Province (*Fairhaead and Maus, 2007; Feng et al., 2007; Brito Neves and Fuck, 2014*); and to the North, the Guanandi Belt - a sequence of Paleoproterozoic rock assemblages reworked during the Brasiliano orogeny - would represent the collisional boundary between the Parnaíba block and the São Luiz-West Africa craton (*Klein et al., 2008*). Some of these lineaments - Transbrasiliano and Araguaia - were identified as deep crustal features in the seismic reflection profile cross-

142 ing the Parnaíba basin, confirming their role as collisional suture zones limiting the central
143 Parnaíba block.

144 Early geophysical studies of the Parnaíba basin, mostly based on data collected during
145 magnetic and/or gravity surveys, delineated a number of graben-like structures concealed un-
146 der the basin's sediments (e.g. *Brito Neves et al., 1984; Nunes, 1993; Cordani et al., 1984*).
147 These interpreted structures were then utilized to support models of thermo-mechanical
148 subsidence for the basin, mostly following the classical model of *McKenzie (1978)*. A most
149 recent refinement of these models of basin formation and evolution was proposed by *de*
150 *Castro et al. (2014)*. From analysis of airborne magnetic and gravimetric anomalies, *de*
151 *Castro et al. (2014)* identified two sets of linear trends in the basement, which were inter-
152 preted as two separate rifting stages - an older one at the end of the Brasiliano orogeny and
153 a younger one in the Cambro-Ordovician - preceding major sag deposition. Interestingly,
154 *Daly et al. (2014)* found no evidence of the early Neoproterozoic phase of rifting postulated
155 by *de Castro et al. (2014)* in their seismic reflection line, and further suggested that the
156 available evidence upon which the younger rift phase was supported could be alternatively
157 interpreted as the signature of pre-Silurian, folded sediments. They also noted that the
158 marked, subplanar unconformity imaged at the base of the Phanerozoic section actually
159 crosses all three crustal blocks (Borborema, Parnaíba and Amazonian), and argued that it
160 might represent a major peneplanation surface. They argue that, if their interpretation were
161 correct, the major boundaries and associated basement structures would have little to do
162 with the formation of the basin and - as the peneplain surface must postdate the complexity
163 of the basement below - thermal subsidence would become a more likely driving mechanism
164 for the formation and evolution of the Parnaíba basin.

165

Data and data processing

166 The dataset utilized in this work was acquired by the Universidade Federal do Rio
167 Grande do Norte and the University of Cambridge as part of the broader Parnaíba Basin
168 Analysis Project (PBAP), a multi-disciplinary effort funded by BP Energy do Brasil that
169 aims at improving our current knowledge of the origin and evolution of this large cratonic
170 basin. The dataset was collected at 9 seismic stations deployed along an approximately EW
171 trending line superimposed to the seismic reflection line of *Daly et al. (2014)*. The stations
172 were interspaced at distances of 50-70 km, covering a total length of ~600 km in the central
173 portion of the basin (see Figure 1). A total of 8 seismic stations were equipped with three-
174 component, Nanometrics Meridian Compact Posthole sensors, with a frequency response flat
175 in velocity between 120 s to 108 Hz, and integrated high-gain digitizers. One station, located
176 in the center of the linear deployment, was equipped with a three-component, Güralp GMT-
177 3T sensor, also with flat response in velocity down to 120 s, and feeding a DM24 digitizer.
178 All stations operated continuously sampling at 100 samples per second and resorted to GPS
179 signal for timekeeping. The central station - contributed by the University of Cambridge -
180 was deployed in August, 2015, while the remaining broadband stations started operations
181 in March, 2016. At the time of submission of this manuscript, all stations were still in
182 operation. Location coordinates and recording time windows considered for analysis in this
183 work are listed in Table 1.

184 In order to develop receiver function estimates for each of the 9 seismic stations in the
185 deployment, seismic sources with epicentral distances between 30° and 90° and magnitudes
186 above 5.5 mb were considered. Receiver functions are obtained by deconvolving the vertical
187 component of the teleseismic P-coda from the corresponding radial component, which effec-

tively removes the signature of the source and instrument response, and leaves the signature of secondary P-to-S converted waves created at seismic discontinuities under the receiver (*Langston, 1979; Ammon, 1991*). Analysis of the amplitudes and travel-times in the receiver functions can then be utilized to develop constraints on the seismic structure under the station (*Owens et al., 1984; Ammon et al., 1990*). Moreover, the deconvolution process equalizes the teleseismic waveforms, which can be stacked to produce high signal-to-noise ratio estimates of the receiver response under a seismic station. The deconvolution procedure can also be applied to the transverse component of the teleseismic P-wave coda. The transverse component should be identically zero for isotropic, laterally homogenous propagating media, so the observation of P-to-S conversions in the transverse receiver function is usually diagnostic for dipping or anisotropic structures under the station (*Cassidy, 1992*).

To effectively compute receiver function estimates, the selected seismograms were cut 10 s before and 120 s after the P-wave arrival, demeaned, detrended, tapered with a 5% cosine window, and band-pass filtered between 0.05 Hz and 5 Hz. The high-pass corner frequency was selected to remove low-frequency noise from the recorded waveforms, while the low-pass corner frequency was chosen to avoid aliasing before re-sampling to 10 samples per second. The decimated waveforms were next rotated into the great-circle-path to obtain the radial and transverse components of ground motion, and low-pass filtered with an acausal Gaussian filter of width 2.5 ($f < 1.25$ Hz). The filtered vertical component was then deconvolved from the corresponding filtered horizontal (radial and transverse) components through the time-domain, iterative scheme of *Ligorria and Ammon (1999)*, with 500 iterations. The deconvolved time series were finally low-pass filtered with a Gaussian filter of width 2.5 to produce the receiver function estimates. A strict quality control was applied to the deconvolved waveforms. First, the radial receiver function was convolved back with the

212 corresponding vertical component to reconstruct the radial component, and those receiver
213 functions not reproducing at least 90% of the original radial component were removed.
214 Second, the transverse receiver functions were visually examined and the radial receiver
215 functions associated to those exhibiting anomalously large amplitudes were excluded from
216 further analysis. Third, the remaining radial receiver functions were visually inspected for
217 outliers, which were also excluded from further analysis. A total of 119 receiver functions,
218 out of 744 waveforms selected for processing, passed our quality control.

219 Average radial and transverse receiver functions for each of the 9 stations considered in
220 this study are displayed in Figure 2. A close inspection of the waveforms reveals important
221 properties about the propagating medium. For instance, the first 3-4 s of the receiver
222 functions are dominated by the signature of the sedimentary cover. Note that the main peak
223 is displaced with respect to the zero lag time, which is the combined effect of a small direct
224 P-wave followed by a large Ps conversion at the sediment-bedrock interface (see e.g. *Zelt and*
225 *Ellis, 1998*). The peak and trough trailing the displaced large amplitude, at lag times around
226 2-3 s, are likely to be multiply reverberated phases between the surface and the sediment-
227 bedrock interface. Luckily, the seismic energy reverberating in the sedimentary layer does
228 not mask the signature of P-to-S conversions from deeper discontinuities. The peak at about
229 5 s lag time is consistent with a Ps conversion at the crust-mantle boundary, and the peak at
230 about 15 s lag time (see e.g. station STSR) is consistent with the first reverberation (PpPs
231 phase) in the crust. The reverberated crustal multiples are nonetheless hard to identify at
232 most of the seismic stations, suggesting a gradational crust-mantle boundary rather than
233 a sharp discontinuity under the sites (see e.g. *Julia, 2007*). The transverse components
234 display amplitudes that are generally small when compared to the corresponding radial
235 components, indicating that lateral variations in structure are small and that the medium

236 under the stations can be regarded as laterally homogeneous. The only exception is station
237 BDCO, which displays a somewhat erratic behaviour with respect to amplitude patterns in
238 the transverse component.

239 Crustal Architecture

240 In this section, we present estimates of crustal thickness, bulk Vp/Vs ratio and 1D profiles
241 of S-velocity variation with depth at individual stations, from analysis of receiver functions
242 obtained for each of the 9 broadband stations in the Parnaíba basin. We also present
243 a migrated receiver function cross-section to image lateral variations in crustal thickness
244 under the profile.

245 Crustal thickness and bulk Vp/Vs ratio

246 Crustal thickness and bulk Vp/Vs ratio can be estimated from receiver functions utilizing
247 the H- κ stacking approach of *Zhu and Kanamori (2000)*. This procedure performs a grid-
248 search over a stacking surface that is built by summing a weighted combination of Ps, PpPs
249 and PpSs+PsPs amplitudes from individual receiver functions. The Ps phase denotes a P-
250 to-S conversion upon refraction across the Moho, while the PpPs and the PpSs+PsPs phases
251 denotes multiple reverberations between the free surface and the Moho containing two P-
252 wave and one S-wave segments and one P-wave and two S-wave segments, respectively (see
253 e.g. *Ammon, 1991*). The summation is performed along the corresponding phase-moveout
254 curves for the three phases, which are computed after assuming a simple layer-over-half
255 space model for the receiving structure. During the calculation, the P-velocity for the layer
256 has to be specified *a priori*, while the thickness and Vp/Vs ratio are left as free parameters.
257 The summation of amplitudes is performed according to

258 $s(H, \kappa) = w_1 \times r(t_1) + w_2 \times r(t_2) - w_3 \times r(t_3)$ (1)

259 where $r(t)$ is the radial receiver function, t_1 , t_2 and t_3 are the predicted Ps, PpPs, and
260 PsPs+PpSs arrival times for the crustal thickness H and Vp/Vs ratio κ , and the w_i are *a*
261 *priori* weighting factors. Crustal thickness and Vp/Vs ratios are varied within prescribed
262 ranges, and the maximum in the $H\text{-}\kappa$ stacking surface is taken as an estimation of crustal
263 thickness and bulk Vp/Vs ratio under the station.

264 Examples illustrating the performance of the $H\text{-}\kappa$ stacking procedure to select stations
265 in the Parnaíba basin are given in Figure 3. The figures display the $H\text{-}\kappa$ stacking surface
266 on the left and the receiver function waveforms, sorted by ray parameter, on the right.

267 In both cases a single local maximum is observed on the $H\text{-}\kappa$ stacking surface, displaying
268 crustal thicknesses of 38.5 ± 0.2 km and 40.9 ± 1.4 km and Vp/Vs ratios of 1.69 ± 0.01 and
269 1.83 ± 0.05 for stations STSR and GRJU, respectively. Confidence bounds were obtained
270 after bootstrapping the receiver function dataset with 200 replications (*Efron and Tibshirani,*
271 1991). Total confidence bounds, nonetheless, will be larger due to uncertainty in the assumed
272 P-wave velocity (see Table 2). At station STSR, the receiver function waveforms display
273 well-defined peaks at around 5, 16, and 20 s, which the algorithm picks as the Ps, PpPs
274 and PpSs+PsPs phases, respectively. At station GRJU, on the other hand, only the Ps
275 conversion is clearly observed in the receiver function waveforms, which translates into larger
276 confidence bounds for the estimated crustal parameters. A close inspection of the receiver
277 functions for station GRJU reveals that the maximum in the $H\text{-}\kappa$ stacking surface seems to
278 be constrained by the negative trough observed at around 22 s in some of the waveforms,
279 which must be kept in mind when interpreting the results at this site.

280 A summary of crustal thicknesses and bulk Vp/Vs ratios for the broadband stations
281 sampling the Parnaíba basin is given in Table 2. In general, we assigned weights of 0.4,
282 0.3, and 0.3 to the Ps, PpPs and PpSs+PsPs phases when they were clearly observed
283 in the receiver function waveforms; however, when one of the multiples was not clearly
284 observed, we assigned a weight of 0.0 to that phase and weights of 0.5 to the remaining
285 phases. As no independent estimates of P-velocity exist for the basin, we opted to base
286 our calculations on the worldwide average of 6.5 km/s derived for continental crust from
287 crustal compilations (*Christensen and Mooney, 1995*) and assess variations in the inferred
288 crustal values for P-velocities varying between 6.3 and 6.7 km/s. The results in Table 2
289 reveals that crustal thicknesses range between 39 and 45 km and are generally constrained
290 within 3-4 km. Vp/Vs ratios are more variable and less well-constrained, although most of
291 the measurements range between 1.69 and 1.76 and have confidence bounds below ± 0.05 .
292 Larger uncertainties are generally related to the number of waveforms available at a given
293 stations and, more specifically, to the consistency of the crustal multiples among waveforms
294 (recall station GRJU in Figure 3).

295 Crustal cross-section

296 Lateral variation in crustal thickness was assessed by building a crustal cross-section
297 through migration and stacking of P-wave receiver functions in the depth domain. We
298 followed the approach of *Frassetto et al (2010)*, which combines the Common Conversion
299 Point (CPP) stacking of *Gilbert and Sheean (2004)* with the phase-weighting scheme of
300 *Schimmel and Paulssen (1997)* to enhance coherent P-to-S conversions during stacking. The
301 geographical locations of the P-to-S conversions - or piercing points - were first tabulated for
302 a range of depths between 0 and 100 km, at 1 km depth intervals, and used to define a grid

303 of uniformly spaced nodes throughout the study area (see Figure 5a). Receiver functions
304 were then back-projected along the Ps ray-paths effectively migrating the receiver functions
305 into the depth domain. Back-projection was achieved after ray-tracing through the 1D
306 velocity model displayed in Figure 5b, which was built by averaging all the S-wave velocity
307 models developed from the joint inversion of receiver functions and surface-wave dispersion
308 presented in the next section. After migration, receiver function amplitudes were stacked
309 with phase weighting within bins containing a minimum of 5 piercing points to produce the
310 crustal cross-section displayed in Figure 5c.

311 The CCP-stacked cross-section displays a major discontinuity at depths of 38-44 km,
312 gently dipping towards the center of the basin, which we interpret as the crust-mantle
313 boundary. No other discontinuities, including the sediment-bedrock interface, are imaged
314 in the cross-section, although some negative amplitudes seem to be mapped at mid-crustal
315 depths. Our inability to image the top of the crystalline basement is mostly a limitation
316 from the low-pass filter applied during receiver function computation ($f < 1.25$ Hz), which
317 cannot separate the Ps conversion at the interface from the direct P-wave (recall Figure 2).
318 The mid-crustal negative amplitudes are artifacts caused by the multiple reverberations
319 between the free-surface and the sediment-bedrock interface, which still stack coherently in
320 the migrated cross-section due to their small phase-moveout.

321 **S-wave velocity-depth profiles**

322 S-wave velocity-depth profiles for each individual station along the transect were de-
323 veloped by inverting the receiver function waveforms developed in this study jointly with
324 independent surface-wave dispersion velocities. We followed the approach of *Julia et al.*
325 (2000; 2003), in which a linear combination of the root-mean-square error for both datasets

326 and a roughness norm for the velocity model are minimized through a linearized, iterative
327 inversion scheme. In that approach, the datasets are equalized for the different number of
328 data points and physical units through normalization by $N\sigma^2$, where N is the number of data
329 points and σ^2 is the data variance, and pre-multiplied by an influence factor ($0 < p < 1$)
330 that controls the relative contribution of each data set to the total norm. Following previous
331 studies (e.g. *Julia et al., 2003; 2008*), we considered an influence factor of 0.5 - giving equal
332 importance to each data set - and average variances of 0.0001 s^{-2} and 0.0025 (km/s)^2 for
333 the receiver functions and dispersion velocities, respectively. In general, 9 iterations sufficed
334 to achieve convergence.

335 The starting model adopted during the inversion consisted of a perfectly elastic, laterally
336 homogeneous and isotropic medium defined through a stack of thin layers of fixed thickness
337 and uniform velocity. The crust has a linear velocity increase from 3.4 km/s at the surface to
338 4.0 km/s at 42.5 km depth, overlying a 4.5 km/s upper mantle. Layer thicknesses are 0.25-
339 1.5 km thick down to 5 km depth - to allow for rapid variations in the sedimentary structure
340 - and then progressively increase from 2.5 km at crustal levels to 5 km in the lithospheric
341 mantle and to 10 km down to 220 km depth, thus reflecting the decrease in resolution with
342 depth associated to the datasets (see e.g. *Julia et al., 2003*). As dispersion velocities have
343 partial sensitivity to deep mantle structure at long periods, the starting model is further
344 parameterized down to \sim 500 km depth with flattened PREM velocities (*Dziewonski and*
345 *Anderson, 1981*), which are constrained to remain unchanged during successive iterations.
346 A flattened PREM might not be the actual structure in the deep mantle under the Parnaíba
347 basin, but will suffice to account for the partial sensitivity of dispersion velocities (see *Julia*
348 *et al., 2003*).

349 Dispersion velocities were borrowed from the continental-scale, surface-wave tomography

study of *Feng et al. (2004)*. In that study, local group-velocity dispersion curves for the fundamental-mode of Rayleigh-waves were developed for periods between 10 and 140 s for the South American continent. Single-station measurements were first taken on the vertical component of regional seismograms - with sources along the plate boundaries and well-recorded at available stations in South America - and then tomographically inverted to develop local dispersion curves within cells that formed a $1^\circ \times 1^\circ$ grid covering the entire continent. The velocity-depth profiles presented in our study were thus developed by jointly inverting the receiver functions developed for a given station with the local dispersion curve associated to the tomographic cell enclosing that station. As we are mainly interested in the crustal architecture of the basin, only dispersion velocities with periods between 10 and 70 s were considered.

The performance of the joint inversion procedure is illustrated in Figure 4 through stations STSN and BUCO, which are located on opposite sides of the transect. The figure displays the starting and final joint inversion models for both stations, along with the fits between observed and predicted receiver functions and Rayleigh-wave dispersion curves. The match between observations and predictions is excellent in both cases, with the fine layering introduced at the top of the model successfully accounting for observed variations in receiver function amplitudes during the first 3-4 seconds in the waveforms. The inverted velocity-depth profiles are simple, and reveal a 38-40 km thick crust with a smooth velocity increase with depth. The sedimentary layers display slow S-velocities in the 1.5-3.0 km/s range down to 2.25 km depth, although sedimentary structure is not tightly constrained in our models due to the lack of short-period dispersion measurements in the dispersion curves. Velocities in the crust vary smoothly with depth, from 3.4-3.5 km/s in the upper crust to values of 4.0-4.1 km/s close to Moho depths. The crust-mantle boundary is modeled as a

374 gradational transition in velocity rather than a sharp discontinuity, as expected from the
375 comparatively small amplitudes displayed by the crustal multiples in comparison to the Ps
376 phase (e.g. *Julia, 2007*). Upper mantle velocities are around 4.5 km/s. Although we did
377 not compute confidence bounds for each individual layer making up the velocity models,
378 typical values are around ± 0.1 km/s for crustal layers and grow towards ± 0.2 km/s as they
379 progress into the mantle (e.g. *Julia et al., 2008*). Confidence bounds for crustal thickness
380 are, at least, one layer thickness (i.e. ± 2.5 km).

381 A summary of the S-velocity models developed for the stations in the Parnaíba basin
382 are displayed in Figure 6. The velocity-depth profiles corroborate the results from the H- κ
383 stacking analysis and the CCP cross-section. The profiles show the crust is 38-42 km thick
384 throughout the basin, with crustal velocities starting at about 3.4-3.5 km/s right under
385 the basin's sediments and smoothly increasing to values of 4.0-4.1 km/s near Moho depths.
386 In the upper mantle, velocities are 4.4-4.5 km/s immediately below the Moho and slowly
387 increase to faster values with depth. The sediment-bedrock interface is located at 2-4 km
388 depth, and sediments display velocities in the 1.5-3.2 km/s range, although - as emphasized
389 above - sedimentary structure is not tightly constrained in our models. Four stations - GRJU,
390 PRDT, STSR, and TRZN - present a relatively high-velocity layer in the upper crust, with
391 peak velocities of 3.7-3.8 km/s in the 5-10 km depth range (2.5-7.5 km at TRZN), but we
392 suspect this is an artifact from insufficient modeling of the shallow sedimentary structure.
393 Geotechnical information from nearby wells - if available - and/or detailed forward modeling
394 of high-frequency receiver functions at those sites will help resolve this issue in the future.
395 In any case, lateral variations in S-velocity and crustal thickness seems to be minimal along
396 the transect. An overlay of all the velocity models was already shown in Figure 5b, which
397 demonstrates that variations in S-velocity and crustal thickness among the Parnaíba seismic

³⁹⁸ stations are within confidence bounds of individual layers.

³⁹⁹ Implications for basin subsidence

⁴⁰⁰ The results on crustal thickness and velocities reported in the previous section reveal
⁴⁰¹ that crustal structure is quite uniform throughout the transect sampled by our seismic
⁴⁰² stations. The crust is 38-42 km thick and has a bulk Vp/Vs ratio in the 1.69-1.76 range,
⁴⁰³ with S-velocities that smoothly increase from 3.4-3.5 km/s under the basin's sediments to
⁴⁰⁴ 4.0-4.1 km/s near Moho depths. A slightly thinner crust is observed under stations STSR
⁴⁰⁵ and BUCO, in agreement with crustal thicknesses reported for the postulated Teresina
⁴⁰⁶ block from gravity modeling (*de Castro et al., 2014*), but those variations are within the
⁴⁰⁷ confidence bounds of our velocity models. Similarly, variations in crustal S-velocity are
⁴⁰⁸ observed among the velocity-depth profiles, but those variations are also within confidence
⁴⁰⁹ bounds (recall Figure 5b). The two instances of Vp/Vs ratios near 1.80 (recall Table 1) are
⁴¹⁰ poorly resolved due to the lack of well-defined multiples. Within uncertainty limits, we can
⁴¹¹ thus conclude that our results are consistent with the presence of a single, uniform crustal
⁴¹² block - the Parnaíba block - concealed under the basin's sediments.

⁴¹³ The crustal thicknesses obtained for the Parnaíba block agree with previous estimates
⁴¹⁴ from independent geophysical (*de Castro et al., 2014; van der Meijde et al., 2013*) and
⁴¹⁵ seismological (*Feng et al., 2007; Lloyd et al., 2010; Assumpção et al., 2013a; 2013b; Uieda
416 and Barbosa, 2017*) studies. It is unfortunate that the seismic reflection line of *Daly et
417 al. (2014)* failed to image the crust-mantle boundary for the Parnaíba block; however,
⁴¹⁸ the smoothness of the velocity-depth profiles developed in our study are consistent with
⁴¹⁹ the lack of reflectivity reported in the active-source profile. Moreover, our velocity-depth
⁴²⁰ profiles also showed that the crust-mantle boundary is a gradational transition rather than

421 a sharp discontinuity, and the inability of the seismic reflection data to image the base
422 of the crust might be related to this transitional character. *Richards* (1972) showed that
423 the P-wave reflection coefficient decays rapidly as the transition interval increases, being
424 $\sim 50\%$ smaller of its maximum value for transitions around $\lambda/4$ (where λ is wavelength).
425 As λ decreases with frequency, it seems plausible that the high-frequency waves utilized in
426 seismic surveys might have difficulties in seeing the full velocity contrast between crust and
427 mantle. Ps conversions, on the other hand, have a weaker $\lambda/2$ dependency on transition
428 thickness (*Bostock*, 1999). As receiver functions sample the Moho with Ps waves, they might
429 have a better chance at imaging gradational boundaries than upper-side P-wave reflections.

430 Our results on crustal thickness are at odds with models of basin evolution that invoke
431 initial mechanical stretching of the basin's lithosphere. According to global compilations
432 (e.g. *Durrheim and Mooney*, 1991; *Zandt and Ammon*, 1995), the crust of Precambrian
433 terrains worldwide is between 35 and 45 km thick. A crustal thickness range of 38-42 km for
434 the Parnaíba block can therefore be regarded as average. Moreover, an average crustal thick-
435 ness indicates that if mechanical stretching occurred before subsidence, the corresponding
436 stretching factor was small. Small stretching factors imply minimal subsidence from initial
437 mechanical stretching and from subsequent cooling of the advected asthenosphere (*McKen-*
438 *zie*, 1978). Thus, a crustal thickness range of 38-42 km, consistent with crustal thickness
439 of outcropping Precambrian terrains worldwide, indicates that mechanical stretching of the
440 Parnaíba basin - if it existed at all - did not play a significant role during its formation and
441 further evolution.

442 The S-velocities variation with depth reported for the Parnaíba block (3.4-4.1 km/s)
443 and the moderate range found for the bulk Vp/Vs ratios (1.69-1.76) are also consistent
444 with the global compilations of velocity structure reported in *Durrheim and Mooney* (1991).

445 According to the compilations, Archean crust is characterized by crustal thicknesses of up to
446 40 km and lacks the presence of a significant layer (> 10 km) of mafic material in the lower
447 crust. According to laboratory measurements in rock samples, typical Vp/Vs ratios for mafic
448 lower crustal lithologies - i.e. mafic granulite and mafic garnet granulite - are around 1.81
449 - 1.82 (*Christensen, 1996*), so a mafic lower crust should increase the bulk Vp/Vs ratio for
450 the entire crustal column. Back-of-the-envelope calculations show that a bulk Vp/Vs ratio of
451 1.76 is compatible with the presence of a layer of 5-6 km of mafic material in the lower crust
452 (see *Luz et al., 2015*); a thicker layer, however, should increase the bulk Vp/Vs ratio above
453 1.76. Moreover, using a P-velocity range of 7.0 - 7.6 km/s for mafic lower crustal material
454 (*Durrhem and Mooney, 1991*) and the Vp/Vs ratios of *Christensen (1996)*, we conclude that
455 S-velocities in the 3.9 - 4.2 km/s range may correspond to mafic rocks. A close inspection of
456 the velocity models in Figure 6 show velocities of 3.9 - 4.1 km/s are reached at the bottom
457 2.5 - 7.5 km of the crust, consistent with our inferences from bulk Vp/Vs ratios.

458 The lack of a massive (> 10 km thick) mafic lower crust under the Parnaíba basin may
459 have implications for understanding the depositional history of this basin. As mentioned
460 before, two magmatic sequences - the Mosquito and Sardinha formations - are found in-
461 terfingering with the lithologies that compose the basin's sediments. Moreover, the Early
462 Cretaceous sequence - the Sardinha formation - has been related to the development of
463 the Central Atlantic Magmatic Province (CAMP), a large igneous province now scattered
464 through the four continents bordering the Atlantic ocean (*Rampino and Stothers, 1988*).
465 *White and McKenzie (1989)* point out that lithospheric stretching will trigger decompres-
466 sion melting of hot asthenospheric mantle, generating melts that will rise passively and in-
467 trude/underplate the overlying crust and modify the buoyancy of the stretched lithosphere.
468 Melt production may double or even quadruple if stretching occurred over abnormally hot

⁴⁶⁹ lithosphere (e.g. as heated by a mantle plume). The small stretching factor inferred from
⁴⁷⁰ our observed crustal thickness implies that magma generation by decompression melting
⁴⁷¹ had to be minimal under the Parnaíba basin, and that the mafic layer making up its lower
⁴⁷² crust is likely not related to the magmatic events recorded in its depositional history. Recall
⁴⁷³ that similar mafic thicknesses are observed in outcropping Precambrian terrains worldwide
⁴⁷⁴ (*Durrheim and Mooney, 1991*), which makes us believe that the origin of the mafic layer is
⁴⁷⁵ not different from that of other Precambrian terrains worldwide.

⁴⁷⁶ Taken at face value, the lack of evidence for mechanical stretching outlined above is con-
⁴⁷⁷ sistent with a purely thermal mechanism driving subsidence in the Parnaíba basin. Thermal
⁴⁷⁸ subsidence, however, might not be the only process capable of explaining subsidence of this
⁴⁷⁹ large cratonic basin of South America. Convection processes in the deep mantle have been
⁴⁸⁰ shown to be capable of triggering vertical movements in the overlying lithosphere, and have
⁴⁸¹ been invoked to explain - for instance - the elevated topography of the South African Plateau
⁴⁸² (e.g. *Lithgow-Berteloni and Silver, 1998; Gurnis et al., 2000*). Similarly, cold-spots asso-
⁴⁸³ ciated with convective downwellings may be capable of explaining the origin of regional
⁴⁸⁴ subsidence (*Hartley and Allen, 1994*). Such downwellings have been invoked to explain the
⁴⁸⁵ subsidence mechanism, for instance, of the Congo basin in Africa (*Downey et al., 2011*).
⁴⁸⁶ After an initial stage of uplift caused by isostatic rebound following delamination, a ver-
⁴⁸⁷ tical downwelling would have been caused by the sinking of the delaminated lithospheric
⁴⁸⁸ fragment, which would in turn drag the overlying lithosphere and cause subsidence of the
⁴⁸⁹ initially elevated region. Determination of lithospheric thickness, as well as imaging of the
⁴⁹⁰ sublithospheric mantle, would be required to assess the plausibility of such mechanisms for
⁴⁹¹ the Parnaíba basin.

⁴⁹² **Conclusions**

⁴⁹³ We have developed 9 point estimates of crustal thickness and bulk Vp/Vs ratio across
⁴⁹⁴ the Parnaíba basin of NE Brazil, along with detailed velocity-depth profiles of S-velocity
⁴⁹⁵ and a migrating cross-section assessing lateral variation of crustal thickness. Our results are
⁴⁹⁶ consistent with the presence of a uniform Precambrian block under the central portion of
⁴⁹⁷ the basin, which is characterized by crustal thicknesses of 38 - 42 km and crustal S-velocities
⁴⁹⁸ smoothly varying between 3.4-3.5 km/s under the basin's sediments and 3.9-4.1 km/s near
⁴⁹⁹ Moho depths. The crustal architecture of the block is similar to that of Precambrian terrains
⁵⁰⁰ worldwide, suggesting minimal stretching of the basin's underlying basement, and conclude
⁵⁰¹ that thermal cooling is a likely mechanism driving basin's subsidence. Deep mantle structure,
⁵⁰² nonetheless, needs to be investigated in order to assess the role of deep convective processes
⁵⁰³ in the formation and evolution of this cratonic basin.

⁵⁰⁴ **Acknowledgements**

⁵⁰⁵ Acquisition and analysis of the dataset presented in this study was funded through
⁵⁰⁶ a grant awarded by BP Energy do Brasil (grant number XXXXXXXXX). Diogo L.O.C.
⁵⁰⁷ additionally thanks BP Energy do Brasil for a generous scholarship to complete his PhD
⁵⁰⁸ degree at the Universidade Federal do Rio Grande do Norte. Jordi Julià also thanks BP
⁵⁰⁹ Energy do Brasil for awarding a research fellowship to conduct this research.

510 References

- 511 Almeida, F.F.M., Hasui, Y., Brito Neves, B.B., Fuck, R.A. (1981). Brazilian structural
512 provinces: An introduction, *Earth Sci. Rev.*, **17**, 1-29.
- 513 Ammon, C.J. (1991). The isolation of receiver effects from teleseismic P waveforms,
514 *Bull. Seism. Soc. Am.*, **81**, 2504-2510.
- 515 Ammon, C. J., Randall, G.E., Zandt, G. (1990). On the non-uniqueness of receiver
516 function inversions, *J. Geophys. Res.*, **95**, 15,303-15,318.
- 517 Assumpção, M., Feng, M., Tassara, A., Julià, J. (2013a). Models of crustal thickness
518 for South America from seismic refraction, receiver functions and surface wave tomography,
519 *Tectonophysics*, **609**, 82-96.
- 520 Assumpção, M., Bianchi, M., Julià, J., Dias, F.L., França, G.S., Nascimento, R.M.N.,
521 Drouet, S., Pavão, C.S., Albuquerque, D.F., Lopes A.E.V. (2013b), Crustal thickness map
522 of Brazil: Data compilation and main features, *J. South Am. Earth Sci.*, **43**, 74-85.
- 523 Bostock, M.G. (1999). Seismic waves converted from velocity gradient anomalies in the
524 Earth's upper mantle, *Geophys. J. Int.*, **138**, 747-756.
- 525 Brito Neves, B.B., Fuck, R.A., Cordani, U.G., Thomas, A. (1984). Influence of basement
526 structures on the evolution of the major sedimentary basins of Brazil: A case of tectonic
527 heritage, *J. Geodyn.*, **1**, 495-510.
- 528 Brito Neves, B.B., Fuck, R.A. (2013). Neoproterozoic evolution of the basement of the
529 South American Platform, *J. South Am. Earth Sci.*, **47**, 72-89.
- 530 Cassidy, J.F. (1992). Numerical experiments in broadband receiver function analysis,
531 *Bull. Seism. Soc. Am.*, **82**, 1453-1474.

- 532 Cloetingh, S., Burov, E. (2011). Lithospheric folding and sedimentary basin evolution:
533 a review and analysis of formation mechanisms, *Basin Res.*, **23**, 257-290.
- 534 Christensen, N. I. (1996). Poissons ratio and crustal seismology, *J. Geophys. Res.*, **101**,
535 3139-3156.
- 536 Christensen, N.I., Mooney, W.D. (1995). Seismic velocity structure and composition of
537 the continental crust: A global view, *J. Geophys. Res.*, **100**, 9761-9788.
- 538 Cordani, U.G., Brito Neves, B.B., Fuck, R.A., Porto, R., Thomaz Filho, A., Cunha,
539 F.M.B. (1984). Estudo preliminar de integração do Pré-Cambriano com os eventos tectônicos
540 das bacias sedimentares brasileiras, *Ciência Técnica Petróleo, Seção Exploração de Petróleo*,
541 Rio de Janeiro 15, p70.
- 542 Cordani, U.G., Brito Neves, B.B., Thomaz Filho, A. (2009). Estudo preliminar de
543 integração do Pré-Cambriano com os eventos tectônicos das bacias sedimentares brasileiras
544 (Atualização), *Bol. Geociênc. Petrobras*, Rio de Janeiro **17** (1), 205-219.
- 545 Cordani, U.G., Pimentel, M.M., Araujo, C.E.G., Fuck, R.A. (2013). The significance of
546 the Transbrasiliano-Kandi tectonic corridor for the amalgamation of West Gondwana, *Braz.*
547 *J. Geol.*, **43**, 583-597.
- 548 Daly, M.C., Andrade, V., Barousse, C.A., Costa, R., McDowell, K., Piggot, N., Poole,
549 A.J. (2014). Brasiliano crustal structure and the tectonic setting of the Parnaíba basin of NE
550 Brazil: Results of a deep seismic reflection profile, *Tectonics*, **33**, doi:10.1002/2014TC003632.
- 551 de Castro, D.L., Fuck, R.A., Phillips, J.D., Vidotti, R.M., Bezerra, F.H.R., Dantas, E.L.
552 (2014). Crustal structure beneath the Paleozoic Parnaíba Basin revealed by airborne gravity
553 and magnetic data, Brazil, *Tectonophysics*, **614**, 128-145.

- 554 Downey, N., Gurnis, M., Avouac, J.-P. (2011). Subsidence history and geodynamic
555 evolution of the cratonic Congo Basin, *Geophys. Res. Abstracts*, **13**, EGU2011-388-1.
- 556 Durrheim, R. J., Mooney, W.D. (1991). Archean and Proterozoic crustal evolution:
557 Evidence from crustal seismology, *Geology*, **19**, 606-609.
- 558 Dziewonsky, A.M., Anderson, D.L. (1981). Preliminary reference earth model, *Phys.
559 Earth Planet. Int.*, **25**, 297-356.
- 560 Efron, B., Tibshirani, R. (1991). Statistical data analysis in the computer age, *Science*,
561 **253**, 390-395.
- 562 Feng, M., Assumpção, M., van der Lee, S. (2004). Group-velocity tomography and
563 lithospheric S-velocity structure of the South American continent, *Phys. Earth Planet.
564 Inter.*, **147**, 315-331.
- 565 Feng, M., Van der Lee, S., Assumpção (2007). Upper mantle structure of South America
566 from joint inversion of waveforms and fundamental-mode group velocities of Rayleigh waves,
567 *J. Geophys. Res.*, **112**, B04312, doi:10.1029/2006JB004449.
- 568 Frassetto, A., Zandt, G., Gilbert, H., Owens, T.J., Jones, C.H. (2010). Improved imaging
569 with phase-weighted common conversion point stacks of receiver functions, *Geophys. J. Int.*,
570 **182**, 368-372.
- 571 Fuck, R.A., Brito Neves, B.B., Schobbenhaus, C. (2008). Rodinia descendants in South
572 America, *Precambrian Res.*, **160**, 108-126.
- 573 Gilbert, A., Sheehan, A.F. (2004). Images of crustal variations in the intermountain
574 west, *J. Geophys. Res.*, **109**, 1978-2012.
- 575 Góes, A. M.O., Feijó, F.J. (1994), Bacia do Parnaíba, *Boletim de Geociências da Petro-*

576 *brás*, **8**, 57-67.

577 Gurnis, M., Mitrovica, J.X., Ritsema, J., van Heijst, H.J. (2000). Constraining mantle
578 density structure using geological evidence of surface uplift rates: The case of the African
579 Superplume, *Geochem. Geophys. Geosyst.*, **1**, 1999GC000035.

580 Hartley, R.W., Allen, P.A. (1994). Interior cratonic basins of Africa: Relation to conti-
581 nental break-up and role of mantle convection, *Basin Res.*, **6**, 95-113.

582 Julià, J., Ammon, C.J., Herrmann, R.B., Correig, A.M. (2000). Joint inversion of re-
583 ceiver functions and surface-wave dispersion ob- servations, *Geophys. J. Int.*, **143**, 99-112.

584 Julià, J., Ammon, C.J., Herrmann, R.B. (2003). Lithospheric structure of the Ara-
585 bian Shield from the joint inversion of receiver functions and surface-wave group velocities,
586 *Tectonophysics*, **371**, 1-21.

587 Julià, J. (2007). Constraining velocity and density contrasts across the crust mantle
588 boundary with receiver function amplitudes, *Geophys. J. Int.*, **171**, 286-301.

589 Julià, J., Assumpção, M., Rocha, M.P. (2008), Deep crustal structure of the Paraná
590 Basin from receiver functions and Rayleigh-wave dispersion: Evidence for a fragmented
591 cratonic root, *J. Geophys. Res.*, **113**, B08318, doi:10.1029/2007JB005374.

592 Kaminski, E., Jaupart, C. (2000). Lithosphere structure beneath the Phanerozoic in-
593 tracratonic basins of North America, *Earth Planet. Sci. Lett.*, **178**, 139-149.

594 Klein, G. deV., A.T. Hsui (1987) Origin of cratonic basins, *Geology*, **15**, 1094-1098.

595 Klein, E.L., Luzardo, R., Moura, C.A.V., Armstrong, R. (2008). Geochemistry and
596 zircon geochronology of Paleoproterozoic granitoids: further evidence on the magmatic and
597 crustal evolution of the São Luís cratonic fragment, Brazil, *Precambrian Res.*, **165**, 221-242.

- 598 Langston, C.A. (1979). Structure under Mount Rainier, Washington, inferred from tele-
599 seismic body waves, *J. Geophys. Res.*, **84**, 4749-4762.
- 600 Ligorría, J.P., Ammon, C.J. (1999). Iterative deconvolution and receiver function esti-
601 mation, *Bull. Seism. Soc. Am.*, **89**, 1395-1400.
- 602 Lithgow-Bertelloni, C., Silver, P.G. (1998), Dynamic topography, plate driving forces,
603 and the African superswell, *Nature*, **395**, 269-273.
- 604 Lloyd, S., van Der Lee, S., França, G.S., Assumpção, M., Feng, M. (2010). Moho map of
605 South America from receiver functions and surface waves, *J. Geophys. Res.*, **115**, B11315,
606 doi:10.1029/2009JB006829.
- 607 Luz, R.M.N., Julià, J., do Nascimento, A.F. (2015). Bulk crustal properties of the
608 Borborema Province, NE Brazil, from P-wave receiver functions: Implications for models of
609 intraplate Cenozoic uplift, *Tectonophysics*, **644-645**, 81-91.
- 610 McKenzie, D. (1978), Some remarks on the development of sedimentary basins, *Earth*
611 *Planet. Sci. Lett.*, **40**, 25-32.
- 612 Nunes, K.C. (1993). Interpretação integrada da Bacia do Parnaíba com ênfase nos dados
613 aeromagnéticos, 3rd International Congress of the Brazilian Geophysical Society, Expanded
614 Abstracts, pp. 152-157.
- 615 Owens, T.J., Zandt, G., Taylor, S.R. (1984). Seismic evidence for an ancient rift be-
616 neath the Cumberland Plateau, Tennessee: a detailed analysis of broadband teleseismic P
617 waveforms, *J. geophys. Res.*, **89**, 7783-7795.
- 618 Rampino, M.R., Stothers, R.B. (1988). Flood Basalt Volcanism During the Past 250
619 Million Years, *Science*, **241**, 663-668.

- 620 Richards, P.G. (1972). Seismic waves reflected from velocity gradient anomalies within
621 the Earth's upper mantle, *J. Geophys.*, **38**, 517-527.
- 622 Schimmel, M., Paulssen, H. (1997). Noise reduction and detection of weak, coherent
623 signals through phase-weighted stacks. *Geophys. J. Int.*, **130**, 497-505.
- 624 Uieda, F., Barbosa V.L.F. (2017). Fast nonlinear gravity inversion in spherical coordi-
625 nates with application to the South American Moho, *Geophys. J. Int.*, **208**, 162-176.
- 626 van der Meijde, M., Julià, J., Assumpçāo, M. (2013). Gravity derived Moho for South
627 America, *Tectonophysics*, **609**, 456-467.
- 628 Vaz, P.T., Rezende, N.A.M., Filho J.R.W., Travassos, W.A.S. (2007). Bacia do Parnaíba,
629 *Boletim de Geociências da Petrobrás*, textbf{2}, 253-263.
- 630 White, R., McKenzie, D. (1989), Magmatism at Rift Zones: The Generation of Volcanic
631 Continental Margins and Flood Basalts, *J. Geophys. Res.*, **94**, 7685-7729.
- 632 Zandt, G., Ammon, C.J. (1995). Continental crust composition constrained by measure-
633 ments of crustal Poisson's ratio, *Nature*, **374**, 152-154.
- 634 Zelt, B.C., Ellis, R.M. (1998). Receiver function studies in the Trans-Hudson orogen,
635 Saskatchewan, *Can. J. Earth Sci.*, **36**, 585-603.
- 636 Zhu, L., Kanamori, H. (2000). Moho depth variation in southern California from tele-
637 seismic receiver functions, *J. Geophys. Res.*, **105**, 2962-2980.

638 **Tables**

Table 1: *Station coordinates and recording time*

window from Parnaíba basin.

Station	Latitude	Longitude	Recording time
BPPF	-6.2271	-47.2518	2016.188 – 2016.345
BUCO	-5.1586	-43.2010	2016.118 – 2016.344
GENI	-5.4612	-45.5344	2016.105 – 2016.346
GRJU	-5.8308	-46.0882	2016.104 – 2016.345
PRDT	-5.3241	-44.3974	2016.106 – 2016.344
STSN	-6.0787	-46.5986	2016.105 – 2016.345
STSР	-5.2889	-43.8063	2016.119 – 2016.344
TRSN	-5.1056	-42.6344	2016.118 – 2016.344
BDCO	-5.4517	-45.0203	2015.222 – 2016.293

Table 2: $H\text{-}\kappa$ stacking parameters and results to different values of V_p from *Parnaíba basin*.

Station	n	w1,w2,w3	H (km) $\pm \epsilon$					Vp/Vs $\pm \epsilon$		
			Vp 6.3	Vp 6.4	Vp 6.5	Vp 6.6	Vp 6.7	Vp 6.3	Vp 6.4	Vp 6.5
30	BPPF	5	0.5,0.5,0.0	41.4 \pm 2.2	42.2 \pm 3.0	42.7 \pm 3.2	43.5 \pm 2.3	44.5 \pm 2.2	1.75 \pm 0.05	1.74 \pm 0.05
	BUCO	11	0.4,0.3,0.3	38.0 \pm 0.8	38.7 \pm 0.7	39.5 \pm 0.8	40.4 \pm 0.9	41.0 \pm 1.4	1.73 \pm 0.03	1.73 \pm 0.02
	GENI	7	0.5,0.5,0.0	43.7 \pm 1.4	44.7 \pm 2.5	45.5 \pm 1.9	46.4 \pm 1.9	47.2 \pm 1.5	1.76 \pm 0.05	1.75 \pm 0.05
	GRJU	11	0.4,0.3,0.3	40.9 \pm 1.8	41.7 \pm 1.9	42.5 \pm 2.2	43.2 \pm 1.7	44.0 \pm 1.3	1.83 \pm 0.05	1.82 \pm 0.05
	PRDT	11	0.4,0.3,0.3	38.7 \pm 3.3	39.5 \pm 3.5	40.2 \pm 3.6	41.0 \pm 3.5	41.9 \pm 3.6	1.81 \pm 0.09	1.80 \pm 0.09
	STSN	12	0.4,0.3,0.3	40.4 \pm 1.8	41.2 \pm 2.2	42.0 \pm 2.5	42.7 \pm 2.6	44.0 \pm 1.5	1.75 \pm 0.04	1.74 \pm 0.05
	STS R	8	0.4,0.3,0.3	38.5 \pm 0.2	39.4 \pm 0.2	40.2 \pm 0.2	40.9 \pm 0.3	41.7 \pm 0.3	1.69 \pm 0.01	1.68 \pm 0.01
	TRSN	12	0.4,0.3,0.3	38.0 \pm 2.8	38.9 \pm 2.8	39.7 \pm 3.0	40.4 \pm 2.8	41.2 \pm 3.3	1.75 \pm 0.07	1.74 \pm 0.07
	BDCO	3	0.4,0.3,0.3	40.0 \pm 3.2	40.7 \pm 3.4	41.5 \pm 3.3	42.5 \pm 3.3	43.2 \pm 3.3	1.70 \pm 0.07	1.69 \pm 0.08

* The table includes the number of waveforms (n), P-wave velocity assumed (Vp), weights for the Ps (w1), PpPs (w2), and PsSs + PsPs (w3) phases, respectively.

639 **Figure Captions**

640 **Fig. 1.** Geological map of the Parnaíba basin displaying the location of Parnaíba
641 Basin Analysis Project (PBAP) stations (triangles) utilized in this study. AM - Amazonian
642 Craton; BB - Borborema Province; SF - São Francisco Craton; SL - São Luís Craton; TO -
643 Tocantins Province.

644 **Fig. 2.** Receiver function stacks developed for the seismic stations in the Parnaíba
645 basin. Right and left panels refer to radial and transversal receiver functions, respectively.
646 The number of waveforms included in the stack are displayed next to the station name in
647 the upper left corner of each panel. The stacks are presented through a black line within
648 a gray shade representing 1σ -confidence bounds for the stacked amplitudes. Although the
649 signature of the sedimentary layers is apparent in the first 3-4 s of the waveforms, it does
650 not seem to interfere with the Ps conversion at ~ 5 s from the crust-mantle boundary.

651 **Fig. 3.** Sample H- κ stacking results for station STSR and GRJU. The left panels display
652 the H κ stacking surfaces, while the right panels display the corresponding radial receiver
653 functions utilized during the stacking procedure. Receiver functions in the right panels were
654 sorted by ray parameter. The thick, black line in panels (a) and (c) is the 1σ -confidence
655 ellipse from bootstrapping, and the thin, dotted lines in panels (b) and (d) are the phase
656 moveout curves for the Ps, PpPs and PpSs+PsPs phases associated to the maximum in the
657 H κ -stacking surface. Note the lack of a consistent PpPs multiple at station GRJU and the
658 correspondingly large uncertainties in the resulting crustal thickness and Vp/Vs ratio.

659 **Fig. 4.** Joint inversion results for statopms STSN and BUCO. The inverted velocity
660 models are shown in the left panels (thick, solid line), along with the starting model utilized
661 in the inversion (thin, solid line). A comparison between observations (gray lines) and

662 predictions (black lines) is given in the middle panels for receiver functions and in the right
663 panels for the dispersion curves. Note the simplicity of the inverted S-velocity profiles and
664 the excellent agreement between observations and predictions, including the large amplitudes
665 in the first 3-4 s in the receiver functions associated to sedimentary structure.

666 **Fig. 5.** Common Conversion Point stacking results for the Parnaíba basin. (a) Map
667 showing the locations of seismic stations (black triangles), nodes considered for the CCP
668 stacking (open circles), and CCP profile (black line); (b) Average S-wave velocity model
669 utilized for migration (back-projection) of the receiver functions; and, (c) CCP stack cross-
670 section displaying stacked receiver function amplitudes, where red colors indicate positive
671 amplitudes (i.e. positive velocity contrast), and blue colors indicate negative amplitudes (i.e.
672 negative velocity contrast). The black marks at \sim 40 km depth are Moho depths estimates
673 obtained from bootstrapping the receiver functions associated to each node along the cross-
674 section. Location of the stations are show on top, superimposed with basin topography.

675 **Fig. 6.** Joint inversion S-velocity models for each station along the profile, sorted
676 according to station location. The models have been shaded according to velocity to display
677 the main layers: sedimentary layer ($V_s < 3.2$ km/s) in white; crust ($3.2 < V_s < 4.3$ km/s) in
678 light gray; and mantle ($V_s > 4.3$ km/s) in dark gray. Dashed line is placed at 3 km depth.
679 H- κ stacking results for crustal thickness are superimposed as vertical lines scaled according
680 to confidence bounds, for comparison. Note the excellent agreement in crustal thickness
681 estimates.

682 Figures

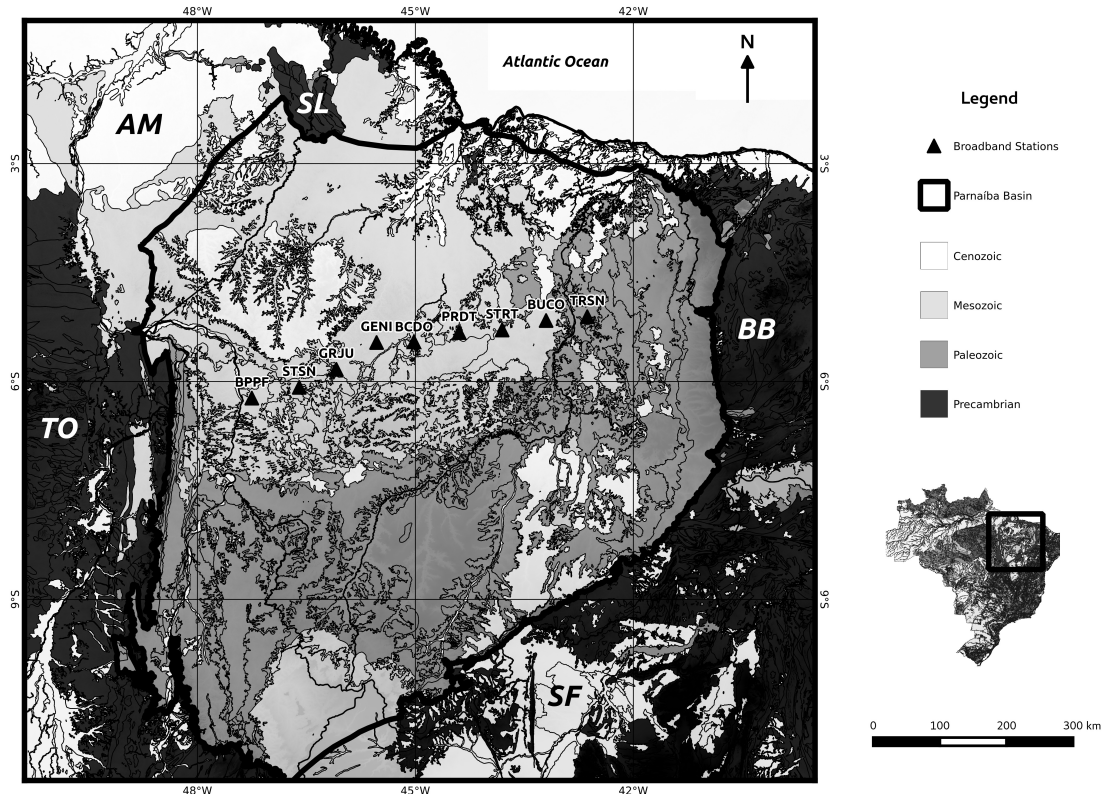


Figure 1: Geological map of the Parnaíba basin displaying the location of Parnaíba Basin Analysis Project (PBAP) stations (triangles) utilized in this study. AM - Amazonian Craton; BB - Borborema Province; SF - São Francisco Craton; SL - São Luís Craton; TO - Tocantins Province.

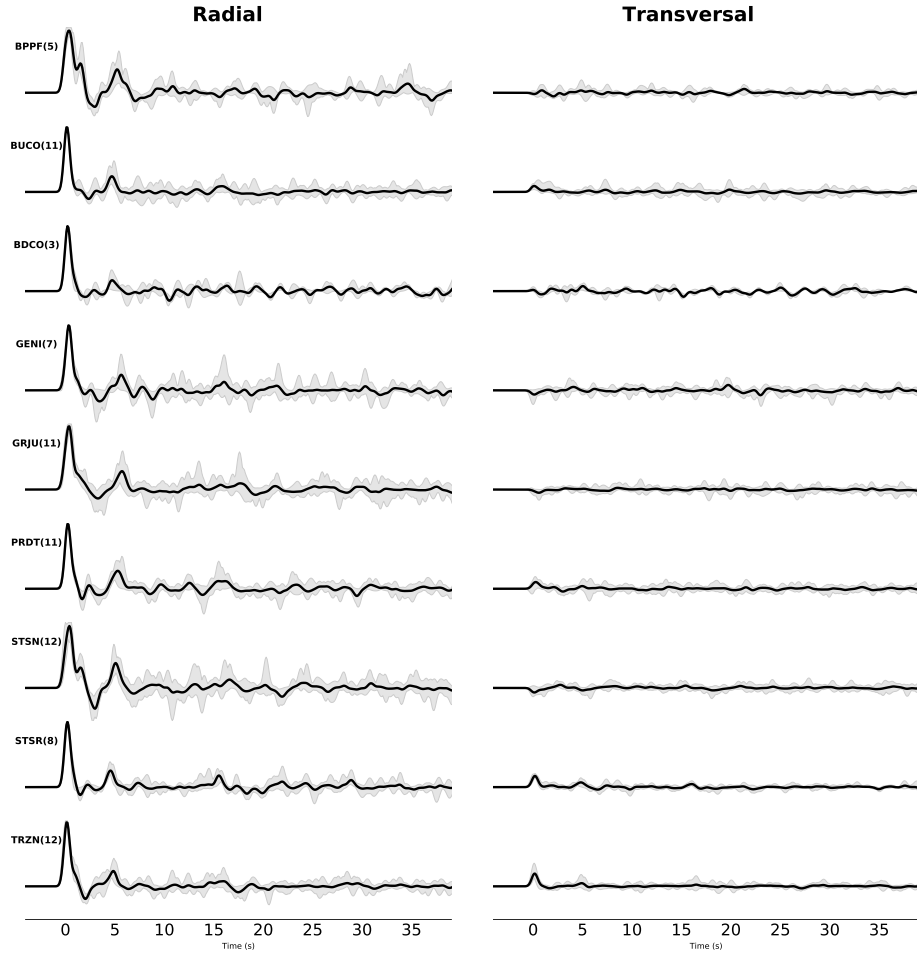


Figure 2: Receiver function stacks developed for the seismic stations in the Parnaíba basin.

Right and left panels refer to radial and transversal receiver functions, respectively. The number of waveforms included in the stack are displayed next to the station name in the upper left corner of each panel. The stacks are presented through a black line within a gray shade representing 1σ -confidence bounds for the stacked amplitudes. Although the signature of the sedimentary layers is apparent in the first 3-4 s of the waveforms, it does not seem to interfere with the P_s conversion at ~ 5 s from the crust-mantle boundary.

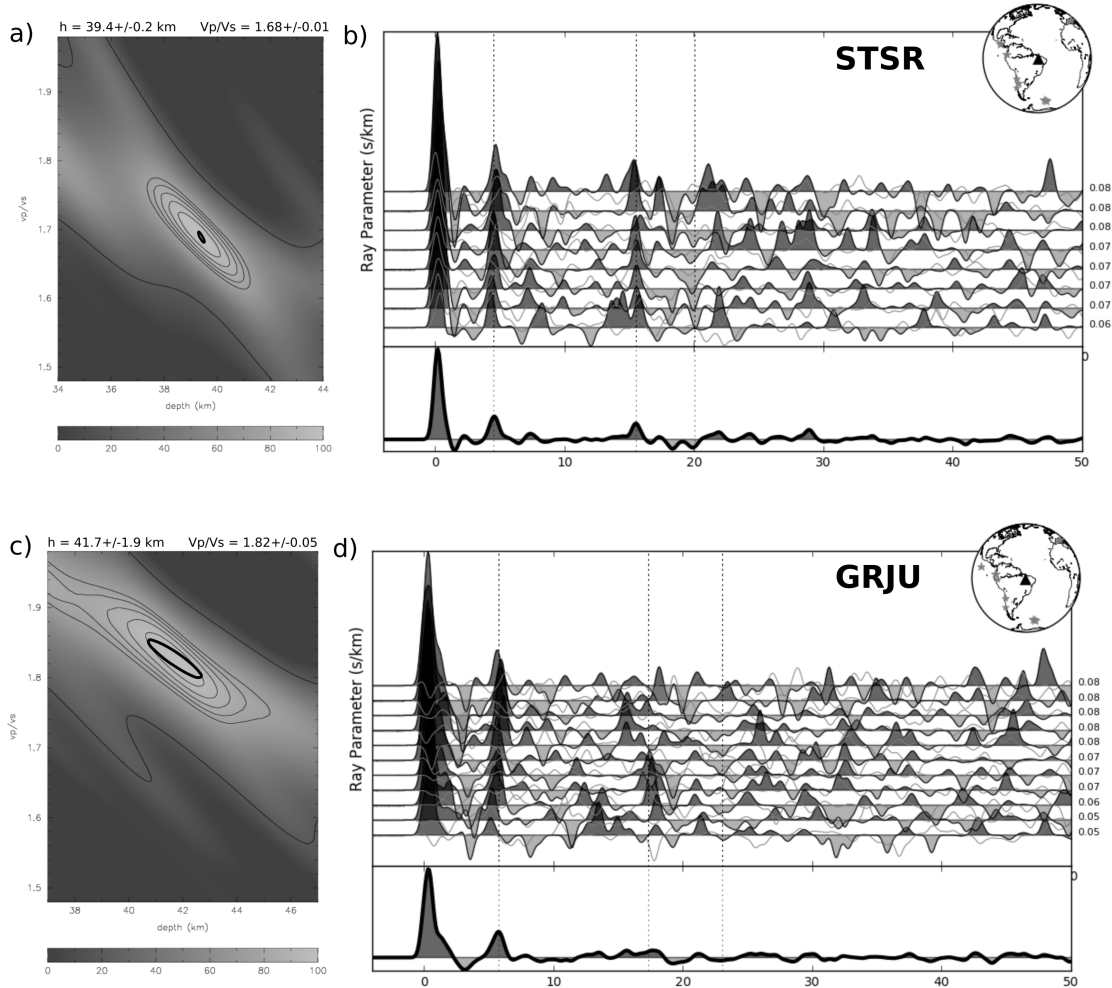


Figure 3: Sample $H\kappa$ -stacking results for station STSR and GRJU. The left panels display the $H\kappa$ stacking surfaces, while the right panels display the corresponding radial receiver functions utilized during the stacking procedure. Receiver functions in the right panels were sorted by ray parameter. The thick, black line in panels (a) and (c) is the 1σ -confidence ellipse from bootstrapping, and the thin, dotted lines in panels (b) and (d) are the phase moveout curves for the Ps , $PpPs$ and $PpSs+PsPs$ phases associated to the maximum in the $H\kappa$ -stacking surface. Note the lack of a consistent $PpPs$ multiple at station GRJU and the correspondingly large uncertainties in the resulting crustal thickness and Vp/Vs ratio.

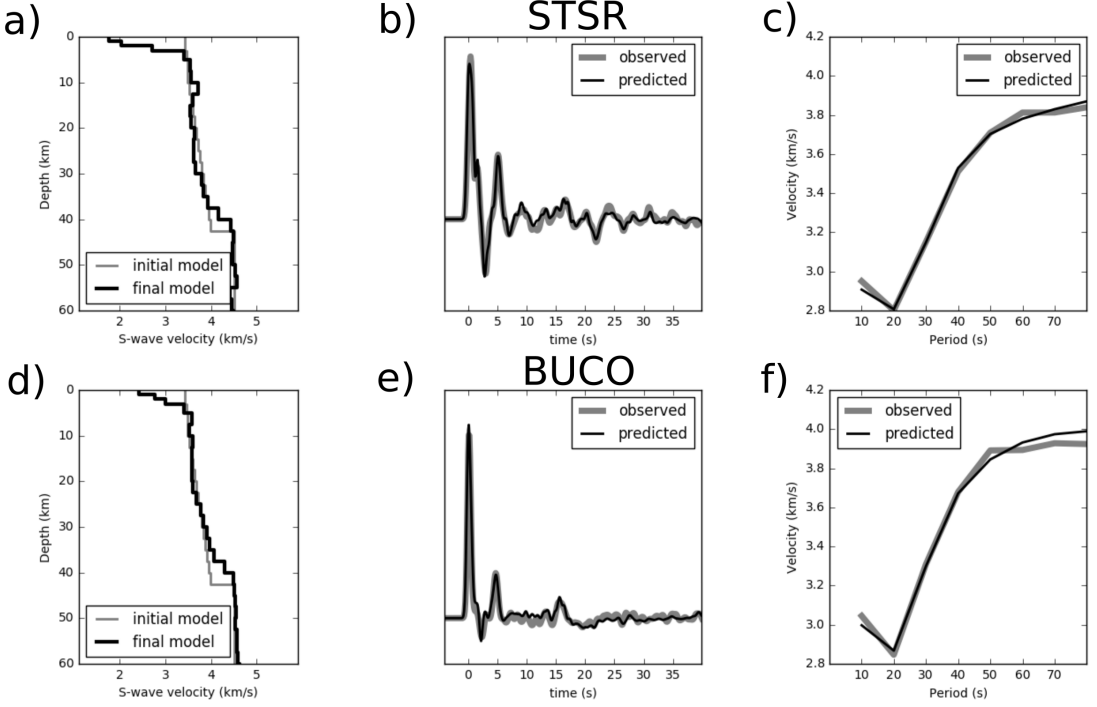


Figure 4: Joint inversion results for statopms STSN and BUCO. The inverted velocity models are shown in the left panels (thick, solid line), along with the starting model utilized in the inversion (thin, solid line). A comparison between observations (gray lines) and predictions (black lines) is given in the middle panels for receiver functions and in the right panels for the dispersion curves. Note the simplicity of the inverted S-velocity profiles and the excellent agreement between observations and predictions, including the large amplitudes in the first 3-4 s in the receiver functions associated to sedimentary structure.

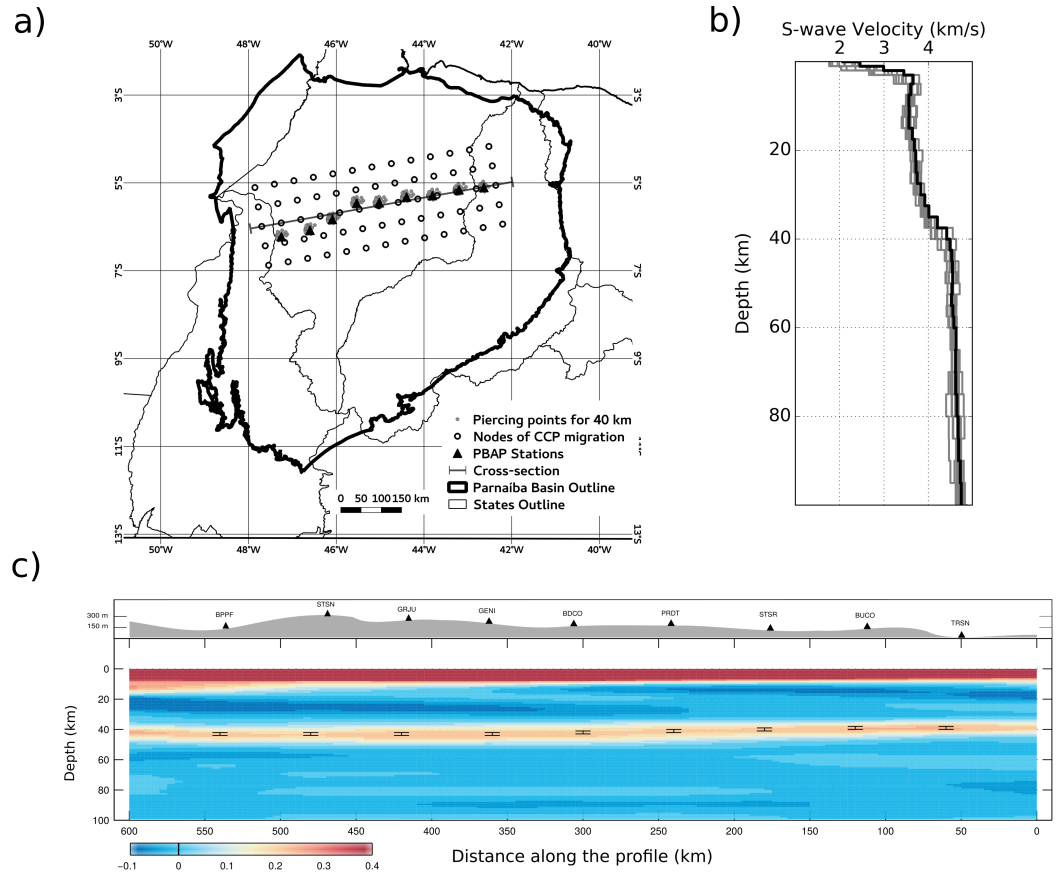


Figure 5: Common Conversion Point stacking results for the Parnaíba basin. (a) Map showing the locations of seismic stations (black triangles), nodes considered for the CCP stacking (open circles), and CCP profile (black line); (b) Average S-wave velocity model utilized for migration (back-projection) of the receiver functions; and, (c) CCP stack cross-section displaying stacked receiver function amplitudes, where red colors indicate positive amplitudes (i.e. positive velocity contrast), and blue colors indicate negative amplitudes (i.e. negative velocity contrast). The black marks at ~ 40 km depth are Moho depths estimates obtained from bootstrapping the receiver functions associated to each node along the cross-section. The location of the stations are shown on top, superimposed with basin topography.

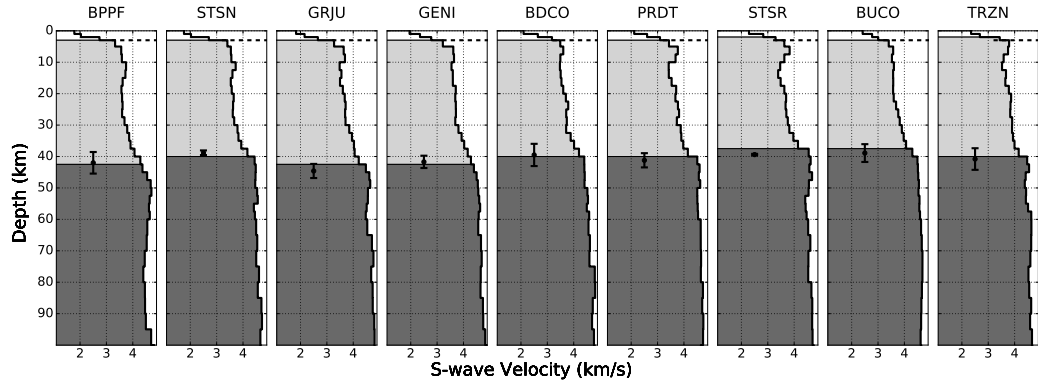


Figure 6: *Joint inversion S-velocity models for each station along the profile, sorted according to station location. The models have been shaded according to velocity to display the main layers: sedimentary layer ($V_s < 3.2 \text{ km/s}$) in white; crust ($3.2 < V_s < 4.3 \text{ km/s}$) in light gray; and mantle ($V_s > 4.3 \text{ km/s}$) in dark gray. Dashed line is placed at 3 km depth. H- κ stacking results for crustal thickness are superimposed as vertical lines scaled according to confidence bounds, for comparison. Note the excellent agreement in crustal thickness estimates.*